Article

Globally Aromatic Odd-Electron π-Magnetic Macrocycle

Federico Villalobos[1,7,†], Jan Berger[2,3,†], Adam Matěj[2,4,†], Reed Nieman[5], Ana Sánchez-Grande[2], Diego Soler[2], Andrés Pinar Solé[2], Hans Lischka[5], Mikuláš Matoušek[6], Jiri Brabec[6], Libor Veis[6], Alba Millan[1], Carlos Sánchez-Sánchez[7], Araceli G. Campaña[1], Juan M. Cuerva[1,*] and Pavel Jelínek[2,3,*]

[1]Departamento Química Orgánica, Universidad de Granada (UGR), Unidad de Excelencia de Química UEQ, C. U. Fuentenueva, 18071 Granada, Spain.

[2]Institute of Physics of the Czech Academy of Sciences, Prague, Czechia.

[3]CATRIN-RCPTM, Palacký University Olomouc, Olomouc, Czechia.

[4]Department of Physical Chemistry, Faculty of Science, Palacký University Olomouc, Olomouc, Czechia.

[5]Department of Chemistry and Biochemistry, Texas Tech University, Lubbock, TX 79409-1061, USA.

[6]J. Heyrovský Institute of Physical Chemistry, Czech Academy of Sciences, Prague, Czechia.

[7]ESISNA Group, Instituto de Ciencia de Materiales de Madrid (ICMM-CSIC), Sor Juana Inés de la Cruz 3, 28049 Madrid, Spain.

† These authors contributed equally to this work

*Correspondence: jmcuerva@ugr.es, jelinekp@fzu.cz

SUMMARY

Molecular π-magnets based on single organic molecules have attracted increasing attention for their potential applications in optoelectronics and spintronics. Global aromaticity in conjugated macrocyclic polyradicaloids is still an open question that has only been tackled in molecules with an even number of electrons. Here, we report the on-surface synthesis of a cyclopenta-ring-fused oligo(*m*-phenylene) macrocycle, **9MC**, with an odd number of electrons. The generated polyradicaloid undergoes a surface-induced distortion to a D_{3h} symmetry with a fully delocalized doublet ground state. Interestingly, **9MC** exhibits two aromatic annulene-within-an-annulene (AWA) ring currents in the inner and outer rings.

Aromaticity, π-magnetism, macrocycles, on-surface synthesis, STS, quantum chemistry calculations

INTRODUCTION

Molecular magnetism has attracted the scientific community's interest during the last years, targeting the design and synthesis of molecular compounds possessing unique magnetic properties and suitable future applications in organic (opto)electronics and spintronics.[1–3] Magnetism at the molecular scale seems simple because molecules with unpaired electrons are, by definition, magnetically active. Nevertheless, the magnetic ground states depend strongly on electron correlation effects. Traditional molecular magnets are based on the presence of metal atoms hosting strongly localized d and f-orbitals hosting unpaired electrons. An alternative route toward molecular magnetism is the concept of π-magnetism.[4] Molecular π-magnets consist of purely hydrocarbon compounds, which can host unpaired electrons in strongly delocalized π-orbitals. Such kind of molecular π-magnets has received much attention due to the progress in the synthesis of polycyclic aromatic hydrocarbons (PAH) in solution[5–7] and on surfaces[8,9] in the last decade. The concept of benzenoid π-magnetism of PAHs is founded on the topological properties of a bipartite lattice,[10] enhanced electron-electron,[11–13] or electron-phonon interactions.[14] Alternatively, π-magnetism can be introduced by incorporating non-benzenoid units.[15–17] Among molecular π-magnets, PAH macrocycles are of special interest, bringing an interesting playground for realizing frustrated antiferromagnetic systems, unusual aromaticity, and the emergence of ring currents.[18] Nevertheless, there is a limited number of studies of π-magnetism in PAH macrocycles due to the difficulties in the design and synthesis of such compounds.

It is also worth noting that the ambiguous concept of aromaticity[19,20] plays an important role in understanding the stability of PAHs. To date, aromatic stabilization by Clar´s aromatic sextet rule[21] in graphene fragments represents a standard way to qualitatively predict the chemical behavior of PAHs, even those containing odd numbers of π-electrons (phenalenyl/olympycenyl radicals, cation, and anion radicals)[22,23] or incorporating five-membered rings in the structure. On the other hand, the influence of the so-called global aromaticity (peripherical ring currents)[18] has been much less explored. Especially relevant is the case of polyradical compounds hosting an annulene-within-an-annulene (AWA) structure consisting of decoupled inner and outer conjugated electronic circuits. The sole examples of such systems are cyclopenta-ring-fused oligo(*m*-phenylene) macrocycles (MCs) with 8 and 10 indene carbocycles (**8MC** and **10MC**), synthesized in solution by the group of Jishan Wu[24] (Figure 1, *even*-MCs). Bulky mesityl groups are introduced for the kinetic stabilization of the radical positions in solution. It is also worth noting that these previous examples present an even number of electrons. The presence of eight (4n electrons, **8MC**) or ten (4n+2, **10MC**) unpaired electrons results in both cases in diatropic inner/diatropic outer ring currents, which is an intriguing situation. Furthermore, the authors also synthesized and characterized nitrogen-substituted **4MC** and **6MC**,[25] demonstrating an increased polyradical character and a singlet ground state. From a fundamental point of view, understanding the role of global aromaticity and AWA in the field of π-magnetism could lead to new magnetic systems with unprecedented properties.

PAH macrocycles with an odd number of π-electrons are fabulous candidates for hosting exotic forms of π-magnetism. We now consider the case of the on-surface synthesis (OSS) of MCs with an odd number of indene units (*odd*-MCs), avoiding the use of bulky protecting

THE BIGGER PICTURE

The electronic structure of the prototypical benzene molecule relays in six p-localized electrons that couple and mix in an antiferromagnetic way generating a stable electronic situation. Similarly, in rigid and planar molecules electrons could mix and couple in a similar way, also resulting in a stable structure. The question appears if an odd number of electrons is considered: is the unpaired electron delocalized in the expected aromatic sense? It is worth noting that the global delocalization should confer to this cyclic radical a chemical inertness compared with other π-radicals. Thus, this particular radical can be considered a kind of superradical. In this work, we present the first example of such kind of radicals based on a unique π-conjugated organic macrocycle with an odd number of π-electrons. It shows π-magnetism with a multiradical doublet ground state and a strongly delocalized SOMO. This special polyradicaloid also presents a global aromaticity with two diatropic ring currents in an annulene-within-an-annulene (AWA) structure, exercising current aromaticity rules. This interesting symmetric molecule can be considered as a magnetic element for the creation of even bigger interconnected cyclic and acyclic magnetic structures with appealing magnetic responses.

groups. Recent advances in the OSS field under ultra-high vacuum conditions (UHV) enabled the synthesis of radical benzenoid and non-benzenoid PAHs on metallic surfaces without the need for protecting groups. Moreover, their chemical and electronic structures can be characterized by high-resolution scanning probe techniques with unprecedented spatial resolution.[26,27] Several works have been reported on Au(111) revealing the structural characterization and the magnetic properties of different PAHs from single molecules (phenalenyl, triangulenes, (peri)acenes or rhombenes) to larger polymers or non-fused macrocycles.[12,28–40]

We envisioned in *odd*-MCs the presence of an antiferromagnetic coupling among radicals in the five-membered rings that may, in principle, enable the formation of frustrated magnetism. The resulting spatial (de)localization of the unpaired electron(s) in conjugated macrocycles is also an interesting question that has not been conclusively addressed. This is not an easy task as OSS-generated carbon-centered radicals placed in five-membered rings are highly localized in the apex positions. Therefore, they present a high tendency to form a covalent bond with the underlying metal surfaces, even with low reactive metals such as gold, requiring the use of insulating NaCl layer(s).[41] In contrast, phenalenyl radical can be considered an archetype magnetic system in which symmetric spin delocalization of the singly occupied molecular orbital (SOMO) level prevents a strong interaction with the underlying metal surface.[39] Within this context, newly designed MC structures require a strategy to deal with the spin localization problem. On the other hand, the synthesis of such *odd*-MCs precursors requires the use of demanding non-symmetric synthetic protocols.

Here, we present the on-surface synthesis of a cyclopenta-ring-fused oligo(*m*-phenylene) macrocycle formed by 9 fused indenes (**9MC**) on the Au(111) surface with an odd number of π-electrons (63 π-e) (Figure 1). This rigid molecule formally exhibits a multiradical doublet ground state, with a marginal energy difference between a full D_{9h} and a reduced D_{3h} symmetry structure. As a result of the adsorption on top of the Au(111) surface, the reduced three-fold symmetry observed experimentally manifests itself in the d*I*/d*V* maps. The SOMO, fully delocalized along the outer rim, confers its unique electronic and chemical properties. We employed high-resolution scanning probe microscopy (SPM) combined with many-body quantum chemistry calculations to determine the electronic ground state of **9MC**. We also discuss the presence of diatropic ring currents within the AWA structure despite the odd number of π-electrons.

Such delocalized currents resemble the electronic behavior of a prototypical benzene molecule in which six p-localized electrons couple and mix in an antiferromagnetic way, generating a stable electronic situation. For highly rigid molecules like the one studied in this work, the electrons mix and couple similarly, resulting in a stable structure in which the unpaired electron is delocalized in the expected aromatic sense (Figure 1). This global delocalization confers chemical inertness to this macrocyclic radical **9MC** compared to other π-radicals such as truxene.[41] These unique features make this macrocyclic radical to be considered as a new kind of *super-radical*.

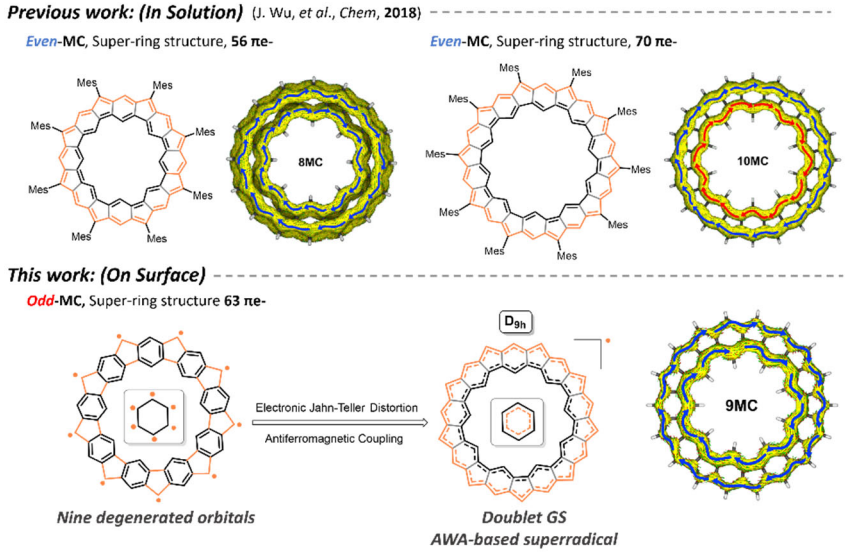

Figure 1. Overview of MCs containing even and odd numbers of electrons

Top: previous in-solution cyclopenta-ring-fused oligo(*m*-phenylene) macrocycles with an even number of electrons. Bottom: new on-surface macrocyclic with an odd number of electrons.

RESULTS AND DISCUSSION

9MC Synthesis

The desired odd π-electron **9MC** is achieved via a two-step on-surface synthesis as summarized in Figure 2. The details of the in-solution synthesis of the macrocyclic precursor **pre-9MC** are included in SI (see Scheme S1). Macrocyclic **pre-9MC** (Figure 2A, left panel) bears nine phenyl rings linked at 1,3-positions and nine methyl substituents for the on-surface generation of nine cyclopenta rings by benzylic C-H bonds activation.[42] The precursor **pre-9MC** was sublimed on a pristine Au(111) surface under UHV conditions with the substrate held at room temperature (RT), resulting in the formation of small aggregates formed by the intact precursor; for more details on sample preparation, see the supplemental information section 1.2. The topography scanning-tunneling microscopy (STM) image in Figure S2 shows such aggregates where the precursor **pre-9MC** has an oval shape with two bright protrusions per molecule.

Subsequent annealing at 280 °C led to the formation of **9H-9MC** (Figure 2A, middle panel). Figure 2B shows an overview topography STM image acquired after the thermal annealing, revealing the circular shape of **9H-9MC** intermediates, predominantly found at the fcc regions of the herringbone reconstruction of Au(111). Figure 2C,D represents constant-height STM (I_t) and high-resolution constant height non-contact atomic force microscopy (nc-AFM) (d*f*) images of **9H-9MC** revealing its inner structure, including five- and six-membered rings and nine bright protrusions corresponding to the CH_2 with one of the hydrogens pointing up. This observation confirms the oxidative ring closure of the nine methyl groups of **pre-9MC**, affording the formation of nine five-membered rings.

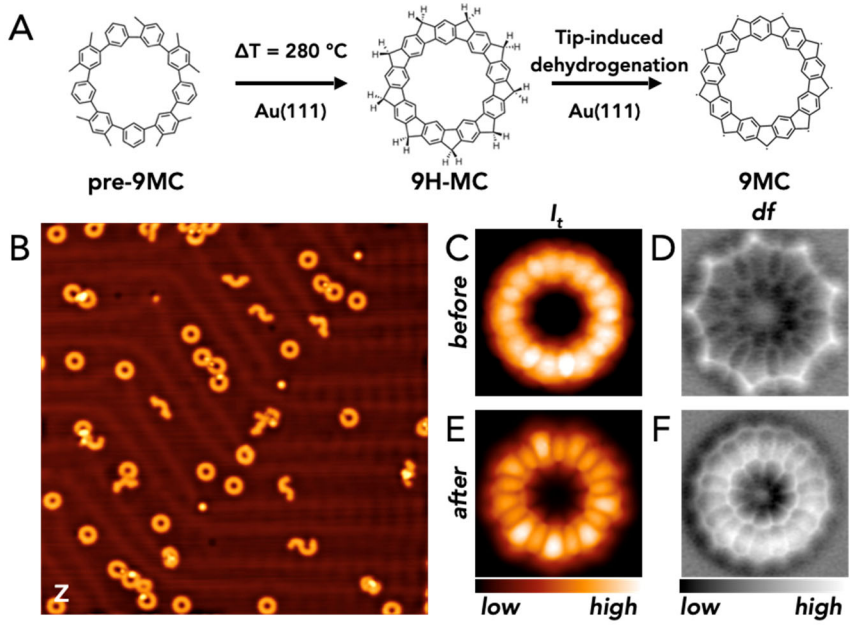

Figure 2. Synthesis and characterization

(A) Schematic view of the two-step on-surface synthesis reaction consisting of the thermal annealing of **pre-9MC** and the selective tip-induced dehydrogenation of the **9H-9MC** intermediates. (B) The topography STM image was taken after the thermal activation of **pre-9MC** by annealing at T = 280 °C for 20 minutes. The products, **9H-9MC** molecules, are visible (closed rings) as well as some broken and not closed fragments. The scanning area is 50 x 50 nm^2, bias voltage U = 50 mV, and tunneling current setpoint I_t = 10 pA. (C) and (D) simultaneously acquired constant height STM (I_t) and nc-AFM (df) images of the **9H-9MC** molecule, respectively. The scanning area is 2.3 x 2.3 nm^2. Bias voltage U = 2 mV. (E) and (F) simultaneously acquired constant height STM and nc-AFM images of the final product, the **9MC** molecule, where the extra hydrogens were removed with the tip from every five-membered ring. The scanning area is 2.3 x 2.3 nm^2. Bias voltage U = 2 mV.

In the next step, we employed tip-induced manipulation to sequentially remove the extra nine hydrogens of the five-membered rings, forming the final product **9MC** (see Figure 2A, right panel). Namely, we positioned the SPM tip over the bright protrusion, in Figure 2D, representing the position of the hydrogen pointing up. Afterward, we gradually increased the bias voltage until a sharp drop in the tunneling current was observed (Figure S3), related to the detaching of the hydrogen from the molecule. A detailed description of the tip-induced dehydrogenation protocol is presented in the supplemental material. Following this procedure, we removed, one-by-one, a hydrogen from all the five-membered rings. Figure 3 displays a sequential series of simultaneously acquired STM and nc-AFM images of the intermediates during the selective one-by-one tip-induced dehydrogenation from the "fully hydrogenated" **9H-9MC** molecule to the final product **9MC**. High-resolution nc-AFM images with a carbon monoxide (CO) tip show that at various stages of the dehydrogenation some dehydrogenated five-membered rings are significantly deformed due to the strong interaction of the apex carbon atom with the metal surface, revealed as a darker contrast over the apical carbon atoms of the five-membered rings in the nc-AFM images. Figure S4 shows some examples of the distortion of different partially dehydrogenated molecules. This indicates a partial instability of the sp^2 configuration of the five-membered rings. Interestingly, after the complete dehydrogenation of all nine five-membered rings, the **9MC** molecule becomes completely planar. This indicates that the formation of the **9MC** macrocycle stabilizes the sp^2 configuration.

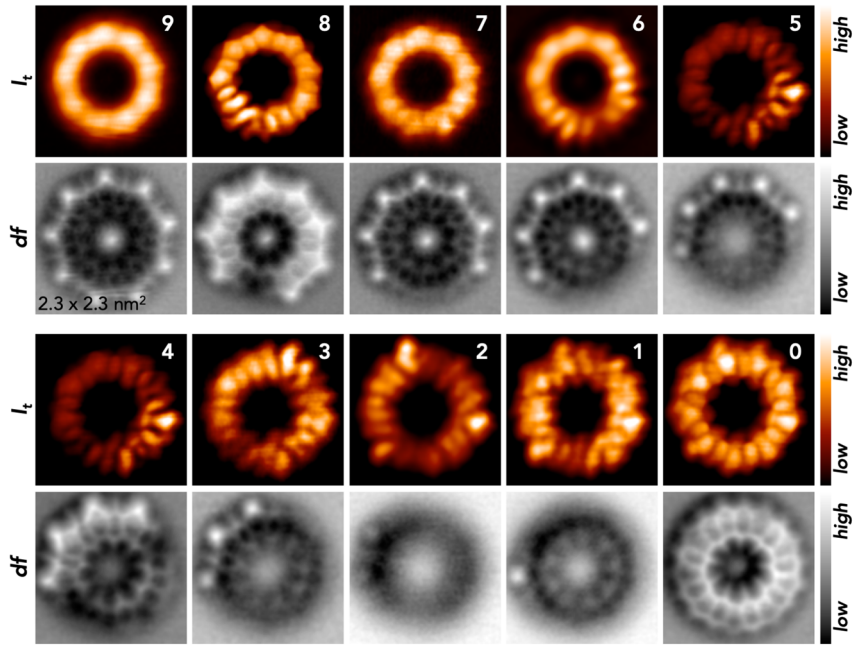

Figure 3. Tip-induced dehydrogenation

Sequence of STM and nc-AFM images along the tip-induced dehydrogenation process. The white numbers in the top-right corner of each STM image represent the number of CH_2 moieties. The scanning area is 2.3 x 2.3 nm^2.

9MC Characterization

Figure 2E,F displays the STM (I_t) and high-resolution nc-AFM (df) images of **9MC**, revealing its planar conformation on the Au(111) surface and a uniform electronic structure. The planar conformation of **9MC** is further demonstrated by df(z) spectroscopy acquired over different positions on the outer and inner rings of the **9MC** molecule, presenting very similar tip-sample distance of the df(z) minimum, proving the planar conformation (Figure S5). Moreover, the difference between the minima of the df(z) curve acquired on the bare Au(111) surface and over **9MC** shows that the molecule lies ~310 pm above the surface, which agrees with a calculated adsorption height of 320 pm obtained from the total energy density functional theory (DFT) calculations with van der Waals correction as shown in Figure S6. Such adsorption height indicates a relatively weak interaction between **9MC** and the Au(111) surface. This scenario is further confirmed by the fact that **9MC** can be laterally moved with the tip without altering its chemical structure, as shown in Figure S7.

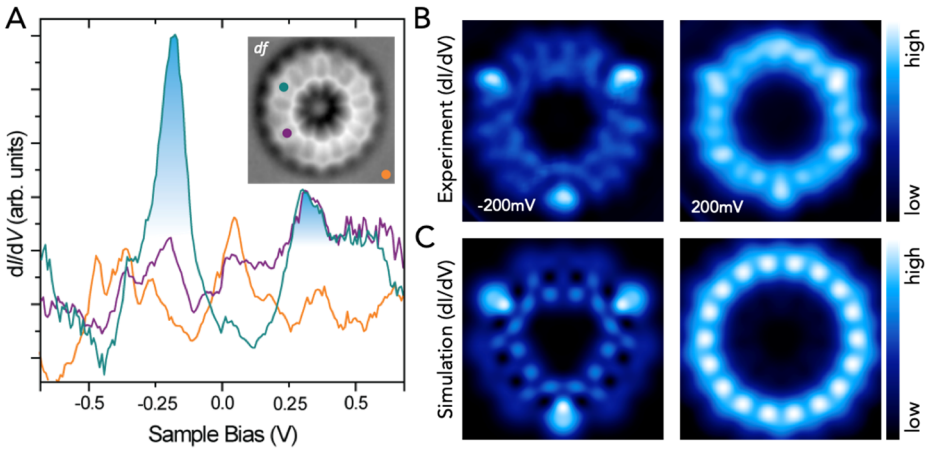

Figure 4. Scanning tunneling spectroscopy

(A) dI/dV point spectra of **9MC**. Acquisition positions are color coded in the nc-AFM inset image. The scanning area of the constant height inset image is 2.4 x 2.4 nm^2. (B) dI/dV maps of **9MC** were taken at bias voltages U = -200 mV (left) and U = 200 mV (right). The typical 3-fold symmetry is visible only at negative voltage. The size of the experimental images is 2.1 x 2.1 nm^2. (C) Simulated dI/dV maps on corresponding Dyson orbitals, vide infra.

To characterize the electronic structure of **9MC**, we employed scanning tunneling spectroscopy (STS) and many-body quantum chemistry calculations. Figure 4A represents characteristic STS data acquired on the **9MC** molecule, revealing a relatively small transport band gap of ~500 meV determined by two resonant states located at -200 and +300 meV, respectively. The constant height dI/dV map acquired at -200 meV shows the characteristic 3-fold symmetry on top of non-adjacent five-membered rings in Figure 4B, left panel. Figure S8 shows that the characteristic 3-fold pattern correlates with the high-symmetry axes of the Au(111) surface, which will play a role as it will be discussed below. On the other hand, the d*I*/d*V* map acquired at +200 meV shows a uniform circular contrast over the **9MC** macrocycle, as shown in Figure 4B, on the right panel.

Theoretical calculations

To rationalize the experimental d*I*/d*V* maps and to gain a more detailed insight into the electronic structure, we carried out total energy DFT and various high-level quantum chemistry calculations, including SC-NEVPT2/CASSCF(9,9), DMRG(63,63), and MRCIS(11,10); for details see supplemental information.

First, we optimized the molecular geometry imposing D_{9h} and D_{3h} symmetries using spin-unrestricted DFT calculations in the gas phase with the TPSS exchange-correlation functional.[43] The D_{3h} structure was obtained by targeting the quartet with the symmetry constraints. At the DFT level, these two geometries are energetically similar, D_{9h} being only 18 meV lower than D_{3h}. Figure S9 displays the optimized structures and their differences, revealing the presence of an AWA structure with bond length alternation within the inner and outer carbon rings interconnected by single C-C bonds. The D_{3h} optimized geometry is very similar in energy to the D_{9h}, keeping the AWA structure with marginal bond length differences.

To understand the effect of the surface, we carried out the spin-polarized total energy DFT PBE[44] with dispersion correction[45] calculations, including the Au(111) substrate. The calculations show that **9MC** adopts a planar configuration at approximately 320 pm above the surface, revealing a weak dispersion interaction with the underlying substrate (see Figure S6) which is in good agreement with the experimental observation (see Figure S5). Importantly, we found that the weak interaction with the surface energetically stabilizes the D_{3h} structure, matching the high symmetry axis of the Au(111) surface. This adsorption position matches with the experimentally observed registry of **9MC** with the underlying Au(111) substrate shown in Figure S8. This observation points toward the effect of a weak interaction with the substrate on the final geometry of **9MC**, i.e., reduction to D_{3h} along the oriented Au(111) surface.

To get more insight into the electronic structure of **9MC**, we then carried out many-body calculations using D_{9h} and D_{3h} structures (for computational details, see 2.1. Methods in supplemental material). In both cases, the ground state is found to be a doublet state, and the natural orbitals (NOs) are practically unchanged between the two geometries. The NOs and their occupation numbers in active spaces for various methods are shown in Figure S10. In the D_{9h} solution, the orbitals degenerate in pairs to give a symmetric electron density according to the molecular symmetry. These degeneracies are lifted for the D_{3h} structure, which is a key observation in connection with the experimentally observed contrast in d*I*/d*V* maps. The electronic structure preserves the same group symmetry as the molecular structure, as illustrated by the above-mentioned degeneracies, which also stays true for the electron transitions. Hence, the excitation processes and the electron abstraction or injection must exhibit the same symmetry. Guided by the experimental evidence of a 3-fold symmetry, we will further focus solely on the electronic structure of the D_{3h} geometry.

To prove the validity of the doublet D_{3h} ground state, we simulated the dI/dV maps to be compared to the experimental evidence. STS measurements correspond to the attachment/detachment of an electron for bias voltage polarities corresponding to empty/occupied states, respectively. Therefore, the observable dI/dV maps correspond to the many-body electronic transition from neutral N to charged N±1 states. To simulate these processes correctly, including reorganization of the electronic structures in charged N±1 states, we adopted the concept of Dyson orbitals[46] representing electron (de)attachment $\left\langle \psi_o^{N\pm1} \middle| \hat{c}^{(+)} \middle| \psi_o^N \right\rangle$ processes that can be directly comparable to dI/dV maps of frontier orbitals, even for strongly correlated molecules.

To obtain Dyson orbitals, shown in Figure 5C, we calculated the charged N±1 ground states $\psi_o^{N\pm1}$. According to NEVPT2/CASSCF(8,9) for N-1 and NEVPT2/CASSCF(10,9) for N+1 calculations, the ground states for charged states are triplet and singlet, respectively, see Figure 5B and supplemental material. The NEVPT2/CASSCF results in a triplet cation ground state, reflecting the CASSCF orbital ordering. Figure 5C shows that the Dyson orbital for electron attachment is very similar to the 9-fold symmetric SONO. Moreover, the calculated d*I*/d*V* map shown in Figure 4C matches the experimental evidence very well.

In the case of the electron detachment, although the resulting first Dyson orbital exhibits a very similar three-fold symmetry to that of the HONO (Figure S12C) it fails in reproducing the correct spatial contrast from the experimental d*I*/d*V* map at negative voltage (Figure S12A). In this regard, only the second Dyson orbital exhibits the correct three-fold symmetry, similar to the HONO-1, which can explain the spatial distribution of the experimental d*I*/d*V* map. Indeed, as seen in Figure S12B, the use of this orbital perfectly matches the experimental d*I*/d*V* map. To understand this inconsistency, we carried out full-π DMRG(63,63) calculations, including all the π orbitals in the active space. The analysis of the occupation numbers shows a good agreement between methods (see Figure S10, S13), supporting the choice of the active space for CASSCF and MRCIS calculations (Figure S10B,C). Moreover, the DMRG orbital ordering swaps the HONO and HONO-1 orbitals compared to CASSCF (see Figure S11). This detail is central to the Dyson orbital calculations. Although the difference in the occupation numbers of these two orbitals is minimal, their swapping is manifested in d*I*/d*V*, vide infra. In summary, Figure 4B,C shows the excellent agreement between experimental and theoretical dI/dV maps. This agreement strongly supports the presence of the doublet ground state in the reduced three-fold symmetry.

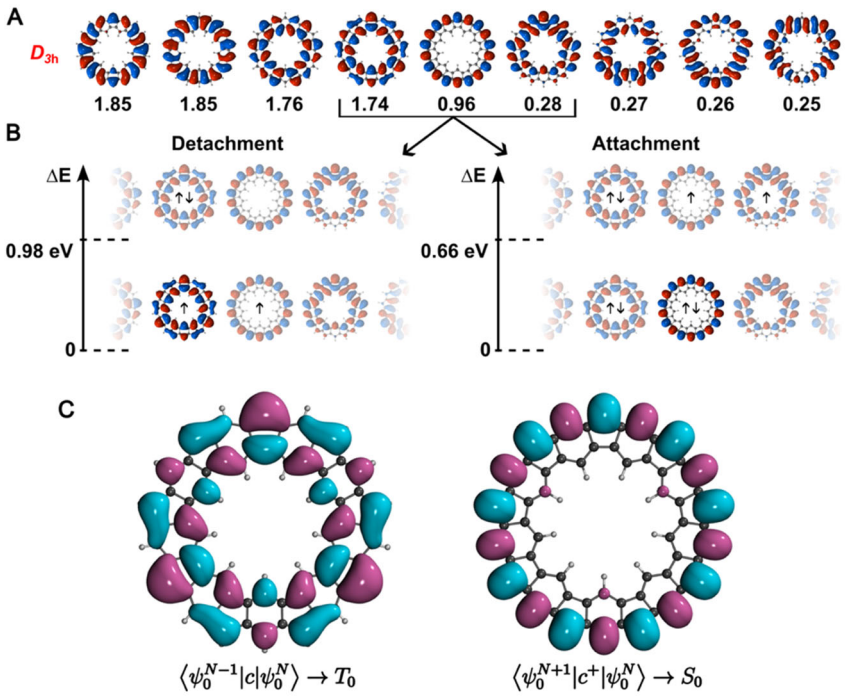

Figure 5. Natural and Dyson orbitals

(A) CASSCF(9,9) natural orbitals of doublet ground state of **9MC** in the D_{3h} symmetry. Occupation numbers and order of NOs are from full-π DMRG calculations. (B) Configurations in N±1 states in natural orbital basis corresponding to Dyson orbitals of electron transfers to N±1 states. Energy scales illustrate the lowest singlet and triplet states. Electron detachment and attachment lead to triplet and singlet ground states, respectively. Natural orbitals that do not change occupancy are translucent, highlighting their absence in the Dyson orbital picture. (C) CASSCF calculated Dyson orbitals from neutral doublet to the charged states.

It is worth noting that according to quantum chemistry calculations, the SONO is strongly delocalized over the whole outer rim of the macrocycle. This strong delocalization of an unpaired electron prevents a strong interaction with the underlying surface. In contrast, highly localized carbon-centered radicals, e.g. in truxene (or indenofluorenes chains)[15,41,47,48] or those presented in partially hydrogenated **9MC**, placed at the five-membered rings tend to form covalent bonds even with low reactive metals such as gold (Figure 3, panels 8 and 4).

Finally, it is worth commenting on the aromatic π-circuits of **9MC**. As a macrocycle with an odd number of π-electrons and an AWA structure, **9MC** offers a rich playground for aromaticity rules. A simple Hückel 4n+2 rule predicts the nonaromatic nature of the macrocycle as a whole and the nonaromatic and antiaromatic nature of the inner and outer rings, respectively (27 and 36 π-electrons, respectively). By looking at the calculated unpaired densities (Figure 6A and S13), it is evident that the unpaired electron resides on the outer rim, suggesting a charge transfer from the inner (hub) to the outer (rim) ring. This leads to a change in aromaticity on individual rings, rendering the inside aromatic with 26 electrons and the outside nonaromatic with 37 electrons. If we continue a step further and consider the 2n+1 aromaticity rule by Mandado[49] and the work by Fowler and colleagues,[50,51] we separate the π-electrons into spin channels on individual AWA rings. The result is illustrated in Figure 6B, which leads to three aromatic and one antiaromatic contribution. Finally, the inner ring is predicted to be fully aromatic, with 13 π-electrons in each spin channel. Conversely, the outer ring bears 19 alpha and 18 beta electrons, demonstrating competition between induced ring currents.

To get further insight into the aromatic character of **9MC**, we performed the analysis of the DFT canonical orbitals and their allowed symmetry operations based on their half-of-azimuthal node count (HANC) labels.[52] The virtual excitations from occupied to virtual orbitals related by translation (ΔHANC=±1) and rotation (ΔHANC=0) contribute to diatropic (aromaticity) and paratropic (antiaromaticity) ring currents, respectively. It can be seen from

Figure S14 that the molecule **9MC** can be described as a globally aromatic AWA macrocycle with only one paratropic interaction on the rim.

We then calculated the anisotropy of the current-induced density (ACID) plots for individual spins and their total plot on the D_{3h} doublet ground state. In the spin-dependent π-ACID plots (Figure 6C,D), there are two conrotating diatropic ring currents in spin alpha. In contrast, spin beta contains diatropic inner and weak paratropic outer ring currents. These results support the discussed decomposition of aromaticity. Figure 6E shows the total π-ACID, revealing the overall appearance of two conrotating diatropic rings and the global aromaticity of **9MC**.

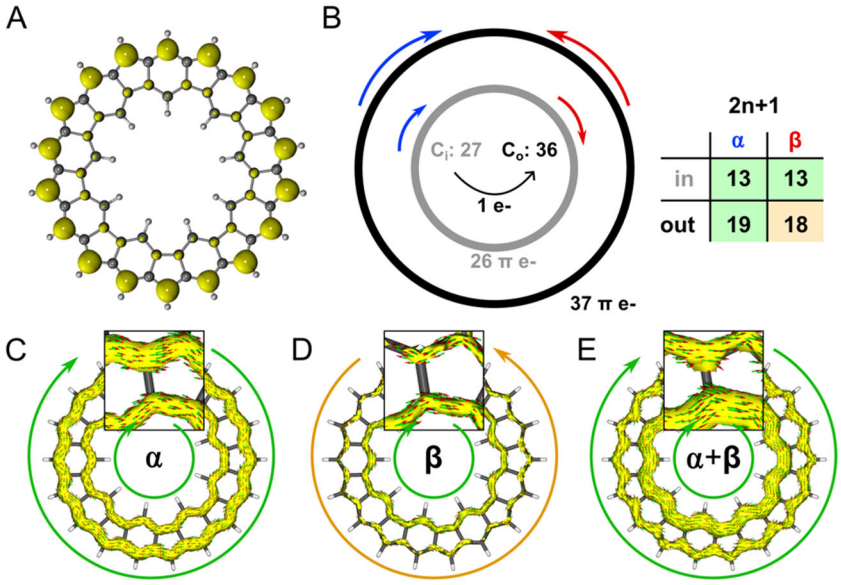

Figure 6. Aromaticity of **9MC**

(A) Unpaired density obtained from NEVPT2/CASSCF(9,9), see Figure S13. (B) Schematic diagram of the decomposition of **9MC** into annulenes and spin channels. The number of carbons in the inner and outer rings is 27 and 36respectively, however, charge transfer leads to the number of π-electrons to be 26 and 37 respectively. The table on the right decomposes these π-electrons into both spins. Mandado's 2n+1 rule then leads to three diatropic and one paratropic ring current. (C) π-ACID plot of alpha-spin orbitals with both rings being diatropic. (D) π-ACID plot of beta-spin orbitals, with the inner ring showing diatropic, and outer paratropic ring currents. (E) Total π-ACID of **9MC**. All four components of the ring current result in the plotted picture.

In conclusion, we have demonstrated the on-surface synthesis of **9MC** with an odd number of π-electrons on the Au(111) surface, which adopts the AWA structure. A combination of *ab initio* methods and experimental measurements sheds light on the complicated description of the electronic structure of **9MC**. We showed that a weak interaction with the underlying surface enables the system to reduce the symmetry. We identify the polyradicaloid doublet ground state with strongly delocalized SOMO orbital. This polyradicaloid doublet with D_{3h} symmetry exhibits two diatropic ring currents, establishing the global aromatic character of **9MC**. We argue that the global aromatic character is responsible for the substantial reduction of the polyradical character of the **9MC** macrocycle.

EXPERIMENTAL PROCEDURES

Resource availability

Lead contact

Further information and requests for resources should be directed to and will be fulfilled by the lead contact, Pavel Jelinek (jelinekp@fzu.cz).

Materials availability

All materials generated in this study are available from the lead contact without restriction.

Data and code availability

All the data supporting the findings of this study are available in the manuscript or in the supplemental information.

SUPPLEMENTAL INFORMATION

Synthetic methods, procedures, on-surface experiments, theoretical calculations and the precursor characterization can be found in the supplemental information online at.

ACKNOWLEDGMENTS

H.L. wants to acknowledge the support of the National Science Foundation [grant number 2107923], Division of Chemistry. Support from the Ministry of Education, Youth and Sports of the Czech Republic through the e-INFRA CZ (ID: 90254). This work received financial support from grant PID2020-113059GB-C21 funded by MCIN/AEI/10.13039/501100011033 and grants PID2021-127521NB-I00 and PID2021-127964NB-C22 funded by MICIU/AEI/ 10.13039/501100011033 and ERDF, EU. F.V. also acknowledges for his FPU contract (FPU18/05938). A.M. acknowledges the support of the Czech Science Foundation (GAČR), project No. 24-10142O. We acknowledge the support of the Czech Science Foundation (GAČR), project No.23-05486S.

AUTHOR CONTRIBUTIONS

Conceptualization, J.M.C., A.G.C., P.J.; Methodology, F.V., J.B., A.M., A.P.S, L.V., R.N., D.S., P.J.; Software, H.L., R.N., A.M., L.V., J.B., M.M.; Formal Analysis, F.V., J.B., A.M., A.S.G., D.S., A.P.S, P.J.; Investigation, J.M.C., A.G.C., A.M., C.S.S., J.B., H.L., L.V., P.J.; Writing – Original Draft, J.M.C., A.G.C., P.J., J.B., A.S., A.M., H.L., L.V.; Funding Acquisition, J.M.C., A.G.C., A.M., C.S.S., H.L., L.V., P.J.; Resources, J.M.C., A.M., P.J., H.L., L.V.; Supervision, J.M.C., A.G.C., H.L., L.V., P.J.

DECLARATION OF INTERESTS

The authors declare no competing interests.

REFERENCES

1. Munárriz, J., Domínguez-Adame, F., and Malyshev, A.V. (2011). Toward graphene-based quantum interference devices. Nanotechnology 22, 365201. https://doi.org/10.1088/0957-4484/22/36/365201.

2. Son, Y.-W., Cohen, M.L., and Louie, S.G. (2006). Half-metallic graphene nanoribbons. Nature 444, 347–349. https://doi.org/10.1038/nature05180.

3. Şahin, H., Senger, R.T., and Ciraci, S. (2010). Spintronic properties of zigzag-edged triangular graphene flakes. J. Appl. Phys. 108, 074301. https://doi.org/10.1063/1.3489919.

4. Yazyev, O.V. (2010). Emergence of magnetism in graphene materials and nanostructures. Rep. Prog. Phys. 73, 056501. https://doi.org/10.1088/0034-4885/73/5/056501.

5. Abe, M. (2013). Diradicals. Chem. Rev. 113, 7011–7088. https://doi.org/10.1021/cr400056a.

6. Lieb, E.H. (1989). Two theorems on the Hubbard model. Phys. Rev. Lett. 62, 1201–1204. https://doi.org/10.1103/PhysRevLett.62.1201.

7. Ovchinnikov, A.A. (1978). Multiplicity of the ground state of large alternant organic molecules with conjugated bonds: (Do Organic Ferromagnetics Exist?). Theor. Chim. Acta 47, 297–304. https://doi.org/10.1007/BF00549259.

8. Song, S., Su, J., Telychko, M., Li, J., Li, G., Li, Y., Su, C., Wu, J., and Lu, J. (2021). On-surface synthesis of graphene nanostructures with π-magnetism. Chem. Soc. Rev. 50, 3238–3262. https://doi.org/10.1039/D0CS01060J.

9. de Oteyza, D.G., and Frederiksen, T. (2022). Carbon-based nanostructures as a versatile platform for tunable π-magnetism. J. Phys. Condens. Matter 34, 443001–443001. https://doi.org/10.1088/1361-648X/ac8a7f.

10. Wang, W.L., Yazyev, O.V., Meng, S., and Kaxiras, E. (2009). Topological Frustration in Graphene Nanoflakes: Magnetic Order and Spin Logic Devices. Phys. Rev. Lett. 102, 157201. https://doi.org/10.1103/PhysRevLett.102.157201.

11. Biswas, K., Soler, D., Mishra, S., Chen, Q., Yao, X., Sánchez-Grande, A., Eimre, K., Mutombo, P., Martín-Fuentes, C., Lauwaet, K., et al. (2023). Steering Large Magnetic Exchange Coupling in Nanographenes near the Closed-Shell to Open-Shell Transition. J. Am. Chem. Soc. 145, 2968–2974. https://doi.org/10.1021/jacs.2c11431.

12. Mishra, S., Yao, X., Chen, Q., Eimre, K., Gröning, O., Ortiz, R., Di Giovannantonio, M., Sancho-García, J.C., Fernández-Rossier, J., Pignedoli, C.A., et al. (2021). Large magnetic exchange coupling in rhombus-shaped nanographenes with zigzag periphery. Nat. Chem. 13, 581–586. https://doi.org/10.1038/s41557-021-00678-2.

13. Song, S., Pinar Solé, A., Matěj, A., Li, G., Stetsovych, O., Soler, D., Yang, H., Telychko, M., Li, J., Kumar, M., et al. (2024). Highly entangled polyradical nanographene with coexisting strong correlation and topological frustration. Nat. Chem. https://doi.org/10.1038/s41557-024-01453-9.

14. González-Herrero, H., Mendieta-Moreno, J.I., Edalatmanesh, S., Santos, J., Martín, N., Écija, D., Torre, B., and Jelinek, P. (2021). Atomic Scale Control and Visualization of Topological Quantum Phase Transition in π-Conjugated Polymers Driven by Their Length. Adv. Mater. 33, 2104495–2104495. https://doi.org/10.1002/adma.202104495.

15. Mishra, S., Vilas-Varela, M., Lieske, L.-A., Ortiz, R., Fatayer, S., Rončević, I., Albrecht, F., Frederiksen, T., Peña, D., and Gross, L. (2024). Bistability between π-diradical open-shell and closed-shell states in indeno[1,2-a]fluorene. Nat. Chem. 16, 755–761. https://doi.org/10.1038/s41557-023-01431-7.

16. Mishra, S., Beyer, D., Berger, R., Liu, J., Gröning, O., Urgel, J.I., Müllen, K., Ruffieux, P., Feng, X., and Fasel, R. (2020). Topological Defect-Induced Magnetism in a Nanographene. J. Am. Chem. Soc. 142, 1147–1152. https://doi.org/10.1021/jacs.9b09212.

17. Biswas, K., Yang, L., Ma, J., Sánchez-Grande, A., Chen, Q., Lauwaet, K., Gallego, J.M., Miranda, R., Écija, D., Jelínek, P., et al. (2022). Defect-Induced π-Magnetism into Non-Benzenoid Nanographenes. Nanomaterials 12, 224–224. https://doi.org/10.3390/nano12020224.

18. Liu, C., Ni, Y., Lu, X., Li, G., and Wu, J. (2019). Global Aromaticity in Macrocyclic Polyradicaloids: Hückel's Rule or Baird's Rule? Acc. Chem. Res. 52, 2309–2321. https://doi.org/10.1021/acs.accounts.9b00257.

19. Merino, G., Solà, M., Fernández, I., Foroutan-Nejad, C., Lazzeretti, P., Frenking, G., Anderson, H.L., Sundholm, D., Cossío, F.P., Petrukhina, M.A., et al. (2023). Aromaticity: Quo Vadis. Chem. Sci. https://doi.org/10.1039/D2SC04998H.

20. Solà, M. (2022). Aromaticity rules. Nat. Chem. 14, 585–590. https://doi.org/10.1038/s41557-022-00961-w.

21. Solà, M. (2013). Forty years of Clar's aromatic π-sextet rule. Front. Chem. 1. https://doi.org/10.3389/fchem.2013.00022.

22. Das, A., Müller, T., Plasser, F., and Lischka, H. (2016). Polyradical Character of Triangular Non-Kekulé Structures, Zethrenes, p -Quinodimethane-Linked Bisphenalenyl, and the Clar Goblet in Comparison: An Extended Multireference Study. J. Phys. Chem. A 120, 1625–1636. https://doi.org/10.1021/acs.jpca.5b12393.

23. Ferrão, L.F.A., Pontes, M.A.P., Fernandes, G.F.S., Bettanin, F., Aquino, A.J.A., Lischka, H., Nachtigallova, D., and Machado, F.B.C. (2023). Stability and Reactivity of the Phenalene and Olympicene Isomers. J. Phys. Chem. A 127, 9430–9441. https://doi.org/10.1021/acs.jpca.3c04331.

24. Liu, C., Sandoval-Salinas, M.E., Hong, Y., Gopalakrishna, T.Y., Phan, H., Aratani, N., Herng, T.S., Ding, J., Yamada, H., Kim, D., et al. (2018). Macrocyclic Polyradicaloids with Unusual Super-ring Structure and Global Aromaticity. Chem 4, 1586–1595. https://doi.org/10.1016/j.chempr.2018.03.020.

25. Das, S., Herng, T.S., Zafra, J.L., Burrezo, P.M., Kitano, M., Ishida, M., Gopalakrishna, T.Y., Hu, P., Osuka, A., Casado, J., et al. (2016). Fully Fused Quinoidal/Aromatic Carbazole Macrocycles with Poly-radical Characters. J. Am. Chem. Soc. 138, 7782–7790. https://doi.org/10.1021/jacs.6b04539.

26. Gross, L., Schuler, B., Pavliček, N., Fatayer, S., Majzik, Z., Moll, N., Peña, D., and Meyer, G. (2018). Atomic Force Microscopy for Molecular Structure Elucidation. Angew. Chem. Int. Ed. 57, 3888–3908. https://doi.org/10.1002/anie.201703509.

27. Hapala, P., Kichin, G., Wagner, C., Tautz, F.S., Temirov, R., and Jelínek, P. (2014). Mechanism of high-resolution STM/AFM imaging with functionalized tips. Phys. Rev. B 90, 085421–085421. https://doi.org/10.1103/PhysRevB.90.085421.

28. Mishra, S., Beyer, D., Eimre, K., Kezilebieke, S., Berger, R., Gröning, O., Pignedoli, C.A., Müllen, K., Liljeroth, P., Ruffieux, P., et al. (2020). Topological frustration induces unconventional magnetism in a nanographene. Nat. Nanotechnol. 15, 22–28.

https://doi.org/10.1038/s41565-019-0577-9.

29. Hieulle, J., Castro, S., Friedrich, N., Vegliante, A., Lara, F.R., Sanz, S., Rey, D., Corso, M., Frederiksen, T., Pascual, J.I., et al. (2021). On-Surface Synthesis and Collective Spin Excitations of a Triangulene-Based Nanostar. Angew. Chem. Int. Ed. 60, 25224–25229. https://doi.org/10.1002/anie.202108301.

30. Mishra, S., Beyer, D., Eimre, K., Liu, J., Berger, R., Gröning, O., Pignedoli, C.A., Müllen, K., Fasel, R., Feng, X., et al. (2019). Synthesis and Characterization of π-Extended Triangulene. J. Am. Chem. Soc. 141, 10621–10625. https://doi.org/10.1021/jacs.9b05319.

31. Zeng, Z., Shi, X., Chi, C., López Navarrete, J.T., Casado, J., and Wu, J. (2015). Pro-aromatic and anti-aromatic π-conjugated molecules: an irresistible wish to be diradicals. Chem. Soc. Rev. 44, 6578–6596. https://doi.org/10.1039/C5CS00051C.

32. Pavliček, N., Mistry, A., Majzik, Z., Moll, N., Meyer, G., Fox, D.J., and Gross, L. (2017). Synthesis and characterization of triangulene. Nat. Nanotechnol. 12, 308–311. https://doi.org/10.1038/nnano.2016.305.

33. Su, J., Telychko, M., Hu, P., Macam, G., Mutombo, P., Zhang, H., Bao, Y., Cheng, F., Huang, Z.-Q., Qiu, Z., et al. (2019). Atomically precise bottom-up synthesis of π-extended [5]triangulene. Sci. Adv. 5. https://doi.org/10.1126/sciadv.aav7717.

34. Mishra, S., Beyer, D., Eimre, K., Ortiz, R., Fernández-Rossier, J., Berger, R., Gröning, O., Pignedoli, C.A., Fasel, R., Feng, X., et al. (2020). Collective All-Carbon Magnetism in Triangulene Dimers**. Angew. Chem. 132, 12139–12145. https://doi.org/10.1002/ange.202002687.

35. Li, J., Sanz, S., Castro-Esteban, J., Vilas-Varela, M., Friedrich, N., Frederiksen, T., Peña, D., and Pascual, J.I. (2020). Uncovering the Triplet Ground State of Triangular Graphene Nanoflakes Engineered with Atomic Precision on a Metal Surface. Phys. Rev. Lett. 124, 177201. https://doi.org/10.1103/PhysRevLett.124.177201.

36. Wang, T., Berdonces-Layunta, A., Friedrich, N., Vilas-Varela, M., Calupitan, J.P., Pascual, J.I., Peña, D., Casanova, D., Corso, M., and De Oteyza, D.G. (2022). Aza-Triangulene: On-Surface Synthesis and Electronic and Magnetic Properties. J. Am. Chem. Soc. 144, 4522–4529. https://doi.org/10.1021/jacs.1c12618.

37. Mishra, S., Xu, K., Eimre, K., Komber, H., Ma, J., Pignedoli, C.A., Fasel, R., Feng, X., and Ruffieux, P. (2021). Synthesis and characterization of [7]triangulene. Nanoscale 13, 1624–1628. https://doi.org/10.1039/D0NR08181G.

38. Su, J., Fan, W., Mutombo, P., Peng, X., Song, S., Ondráček, M., Golub, P., Brabec, J., Veis, L., Telychko, M., et al. (2021). On-Surface Synthesis and Characterization of [7]Triangulene Quantum Ring. Nano Lett. 21, 861–867. https://doi.org/10.1021/acs.nanolett.0c04627.

39. Turco, E., Bernhardt, A., Krane, N., Valenta, L., Fasel, R., Juríček, M., and Ruffieux, P. (2023). Observation of the Magnetic Ground State of the Two Smallest Triangular Nanographenes. JACS Au 3, 1358–1364. https://doi.org/10.1021/jacsau.2c00666.

40. Ruffieux, P., Wang, S., Yang, B., Sánchez-Sánchez, C., Liu, J., Dienel, T., Talirz, L., Shinde, P., Pignedoli, C.A., Passerone, D., et al. (2016). On-surface synthesis of graphene nanoribbons with zigzag edge topology. Nature 531, 489–492. https://doi.org/10.1038/nature17151.

41. Mishra, S., Fatayer, S., Fernández, S., Kaiser, K., Peña, D., and Gross, L. (2022). Nonbenzenoid High-Spin Polycyclic Hydrocarbons Generated by Atom Manipulation. ACS Nano 16, 3264–3271. https://doi.org/10.1021/acsnano.1c11157.

42. Xu, X., Di Giovannantonio, M., Urgel, J.I., Pignedoli, C.A., Ruffieux, P., Müllen, K., Fasel, R., and Narita, A. (2021). On-surface activation of benzylic C-H bonds for the synthesis of pentagon-fused graphene nanoribbons. Nano Res. 14, 4754–4759. https://doi.org/10.1007/s12274-021-3419-2.

43. Tao, J., Perdew, J.P., Staroverov, V.N., and Scuseria, G.E. (2003). Climbing the Density Functional Ladder: Nonempirical Meta–Generalized Gradient Approximation Designed for Molecules and Solids. Phys. Rev. Lett. 91, 146401. https://doi.org/10.1103/PhysRevLett.91.146401.

44. Perdew, J.P., Burke, K., and Ernzerhof, M. (1996). Generalized Gradient Approximation Made Simple. Phys. Rev. Lett. 77, 3865–3868. https://doi.org/10.1103/PhysRevLett.77.3865.

45. Tkatchenko, A., and Scheffler, M. (2009). Accurate Molecular

Van Der Waals Interactions from Ground-State Electron Density and Free-Atom Reference Data. Phys. Rev. Lett. 102, 073005. https://doi.org/10.1103/PhysRevLett.102.073005.

46. Ortiz, J.V. (2020). Dyson-orbital concepts for description of electrons in molecules. J. Chem. Phys. 153, 070902–070902. https://doi.org/10.1063/5.0016472.

47. Zhao, C., Huang, Q., Valenta, L., Eimre, K., Yang, L., Yakutovich, A.V., Xu, W., Ma, J., Feng, X., Juríček, M., et al. (2024). Tailoring Magnetism of Graphene Nanoflakes via Tip-Controlled Dehydrogenation. Phys. Rev. Lett. 132, 046201. https://doi.org/10.1103/PhysRevLett.132.046201.

48. Di Giovannantonio, M., Eimre, K., Yakutovich, A.V., Chen, Q., Mishra, S., Urgel, J.I., Pignedoli, C.A., Ruffieux, P., Müllen, K., Narita, A., et al. (2019). On-Surface Synthesis of Antiaromatic and Open-Shell Indeno[2,1- b]fluorene Polymers and Their Lateral Fusion into Porous Ribbons. J. Am. Chem. Soc. 141, 12346–12354. https://doi.org/10.1021/jacs.9b05335.

49. Mandado, M., Graña, A.M., and Pérez-Juste, I. (2008). Aromaticity in spin-polarized systems: Can rings be simultaneously alpha aromatic and beta antiaromatic? J. Chem. Phys. 129, 164114. https://doi.org/10.1063/1.2999562.

50. Steiner, E., Fowler, P.W., and Jenneskens, L.W. (2001). Counter-Rotating Ring Currents in Coronene and Corannulene. Angew. Chem. Int. Ed. 40, 362–366. https://doi.org/10.1002/1521-3773(20010119)40:2<362::AID-ANIE362>3.0.CO;2-Z.

51. Steiner, E., and Fowler, P.W. (2001). Four- and two-electron rules for diatropic and paratropic ring currents in monocyclic ï€ systems. Chem. Commun., 2220–2221. https://doi.org/10.1039/b104847n.

52. Summa, F.F., Zanasi, R., Đorđević, S., Radenković, S., and Monaco, G. (2024). On the Unusual Global Aromaticity of Two Cyclopenta-Ring-Fused Oligo(m-Phenylenes). ChemPhysChem, e202400342. https://doi.org/10.1002/cphc.202400342.